Spatio-temporal dynamics in fMRI recordings revealed with complex independent component analysis

Jörn Anemüller*, Jeng-Ren Duann, Terrence J. Sejnowski, and Scott Makeig

Swartz Center for Computational Neuroscience, Institute for Neural Computation,
University of California San Diego, La Jolla, California, and
Computational Neurobiology Laboratory,
The Salk Institute for Biological Studies, La Jolla, California, and
Howard Hughes Medical Institute

Abstract. Independent component analysis (ICA) of functional magnetic resonance imaging (fMRI) data is commonly carried out under the assumption that each source may be represented as a spatially fixed pattern of activation, which leads to the instantaneous mixing model. To allow modeling patterns of spatio-temporal dynamics, in particular, the flow of oxygenated blood, we have developed a convolutive ICA approach: spatial complex ICA applied to frequency-domain fMRI data. In several frequency-bands, we identify components pertaining to activity in primary visual cortex (V1) and blood supply vessels. One such component, obtained in the 0.10-Hz band, is analyzed in detail and found to likely reflect flow of oxygenated blood in V1.

1 Introduction

The blood oxygenation level dependent (BOLD) contrast measured by fMRI recordings depends on the change in level of oxygenated blood with neural activity. ICA has been successful at finding independent spatial components that vary in time [1,2], but there may also be spatio-temporally dynamic patterns in fMRI recordings of brain activity.

Convolutive models are a way to account for dynamic flow patterns. In convolutive models, each source process is characterized by the spatio-temporal pattern it elicits and by the time-course of activation of this pattern. The signal accounted for by each source process is obtained by convolving the spatio-temporal source pattern with its time-course of activation. The mixed (measured) data are obtained by summing over the contributions of all source processes. Separation of mixed activity generated by several of such processes is not possible for instantaneous ICA algorithms since the convolutive mixing is beyond the scope of their instantaneous mixing assumption.

The convolutive separation problem can be solved by performing all computations in the frequency-domain since the convolution in the time-domain factorizes into a multiplication in the frequency-domain. Separation is performed by applying a complex ICA algorithm to the complex-valued data in each frequency-band.

The use of this procedure for the analysis of electroencephalographic (EEG) data has recently been presented elsewhere [3]. Here, we present the application of the

* present address: Dept. of Physics, Medical Physics, University of Oldenburg, 26111 Oldenburg, Germany

method to fMRI data. Compared to EEG data, fMRI data are characterized by their high spatial resolution at a low temporal sampling rate. fMRI data are commonly analyzed by spatial ICA decomposition, where time-points correspond to input dimensions and voxels to samples. This is in contrast to temporal ICA used for EEG, where sensors constitute input dimensions and time-points samples. To apply complex ICA to fMRI signals, we similarly apply spatial complex ICA to frequency-domain fMRI data.

2 Methods

Convolutive ICA models have traditionally been in use to perform blind separation of acoustically recorded signals into individual sources (e.g., several speakers, or speaker and noise source, [4,5,6]). The convolutive mixing model comes into play through room acoustics, where the signal of each speaker has to be convolved with the room's impulse response from the speaker to each of the microphones to obtain the signal at each microphone. The convolution captures the effects of the acoustic environment to delay the sound signal during its propagation from speaker to microphone, and to generate echoes of the direct sound. At the sensor arrays, one speaker's signal in general arrives earlier (or later) at one microphone than at other microphones, which may be interpreted as a spatial and temporal variability that is introduced into the signal by convolution.

In the present contribution, we generalize from the physical underpinnings of acoustic wave propagation, and use the convolutive signal propagation and superposition model to capture spatial and temporal dynamics in brain sources measured with a quasi-instantaneous measuring process. We do *not* use convolution to model the physics of the electromagnetic wave signal propagation, but to endow the underlying source processes with the potential for both spatial and temporal dynamics compatible with the neuronal and biological substrate of the observed brain processes.

For a toy example, refer to Fig. 1, where a delta-shaped source activation is convolved with several impulse responses from the source to different voxels. The impulse responses essentially correspond to a set of different delays (together with a temporal smearing) and give rise to the sensation of a moving pattern that changes its spatial position at the voxels with time: a spatio-temporally dynamic source process. Note that while a single source is sufficient to account for the process with a convolution model, this would not be possible with an instantaneous (i.e., multiplicative but not convolutive) model. At best, multiple spatially fixed source processes, with mutually different spatial foci and shifted temporal activations, could achieve a similar goal, however, sacrificing their independence and artificially inflating the number of sources.

For the separation of several spatio-temporal dynamic sources, different source activations each with a different set of impulse responses would be used. From the sensor data, it is only possible to reconstruct the source activation up to an unknown convolution: In our toy example, the "temporal smearing" could be incorporated into the source activation rather than the impulse responses of the sensors without changing the voxel signals. Despite this ambiguity, the pattern each individual source evokes at the voxels is uniquely determined.

Under convolutive ICA, the usual concept of a spatially fixed source is replaced by a more abstract source process with spatial and temporal dynamics, and our goal

is to isolate portions of the recorded data attributable to individual source processes. However, a source process can in any case only be observed by means of the signals it contributes to the measurement, i.e., the spatial and temporal voxel activation patterns produced by the source process (corresponding in our acoustic analog to that part of the acoustic signal recorded at all microphones produced by an individual speaker). The source activation (e.g., the speaker's vocal source signal) may not have a concrete biological counterpart in the analysis of brain signals.

We note that the use of convolutive models to extract components with spatio-temporal dynamics should not be confused with the "spatiotemporal ICA" method [7], that extracts static (non-convolutive) components using an instantaneous mixing model.

Because of the equivalence of time-domain convolution and frequency-domain multiplication, the convolutive source superposition can be expressed in the frequency-domain as a multiplication of spectral representations of measured signals, source activations, and impulse responses. As spectral transforms of all three quantities are in general complex-valued, a complex ICA method [3,8] is used to separate the time-frequency representations of the voxel activations into independent components. The main steps of the method are illustrated in Fig. 2.

Consider measured signals x_{ti}, where t denotes time and i denotes voxels. Their spectral time-frequency representations $x_{Ti}(f)$ are computed using the short-term Fourier transformation

$$x_{Ti}(f) = \sum_{\tau} x_i(T+\tau)h(\tau)\, e^{-\mathrm{i}2\pi f\tau/2K} \tag{1}$$

where f denotes center frequency, and $h(\tau)$ is a Hanning window centered at time T. Usually, spectral transforms are computed at a subset of time-points ("T") of the original time-domain data measurements (indicated by "t"). Hence, data of size [times t $\times$ voxels i] are transformed into data of size [times T $\times$ voxels i $\times$ frequencies f].

For each frequency band f, the signals are modeled to be generated from independent sources $s_{Ti}(f)$ by multiplication with frequency-specific mixing coefficients $a_{TT'}(f)$,

$$x_{Ti}(f) = \sum_{T'} a_{TT'}(f)\, s_{T'i}(f), \tag{2}$$

which in matrix notation reads

$$\mathbf{X}(f) = \mathbf{A}(f)\,\mathbf{S}(f). \tag{3}$$

Complex ICA separates the data into independent components using the linear projection

$$\mathbf{U}(f) = \mathbf{W}(f)\,\mathbf{X}(f), \text{ i.e.,} \tag{4}$$

$$u_{Ti}(f) = \sum_{T'} w_{TT'}(f)\, x_{T'i}(f), \tag{5}$$

where $u_{Ti}(f)$ and $w_{TT'}(f)$ represent complex spatial component patterns and the separating matrix, respectively.

Hence, as in real-valued ICA for fMRI signals, a spatial ICA decomposition is performed, where time-points correspond to input dimensions and voxels to samples. For

each frequency-band, we obtain a set of complex-valued independent components, their number limited by the number of temporal windows T'. Each is characterized by its associated complex time-course $\mathbf{a}_{T'}(f)$ and complex-valued spatial pattern $\mathbf{s}_{T'}(f)$, with T' denoting component number.

The complex ICA algorithm employed here is a generalization of the real-valued infomax ICA algorithm [9] and was first derived via a maximum-likelihood approach [10], for a detailed exposition see [3,8]. The resulting update rule was proposed earlier, albeit without derivation, by [11], and later derived independently by [12,13]. Alternative complex ICA algorithms have been proposed by, e.g., [14,15,16,17].

The derivation of the complex infomax algorithm employed is briefly summarized below. Sources are modeled as complex random variables with a circular symmetric, super-Gaussian probability density function. Because of circular symmetry, the probability density corresponding to the complex source value s depends only on the (real-valued) magnitude $|s|$ of s,

$$\mathcal{P}_s(s) = g(|s|). \tag{6}$$

The assumption of a super-Gaussian pdf results in the real and imaginary parts of s *not* being independent of each other. Analysis of the statistics of frequency-domain fMRI data exhibits a positive kurtosis and strongly indicates that these assumptions are fulfilled.

Matrices $\mathbf{W}(f)$ are found by maximizing the log-likelihood $L(\mathbf{W}(f))$ of the measured signals $\mathbf{X}(f)$ given $\mathbf{W}(f)$, which in terms of the source distribution $\mathcal{P}_s$ is

$$L(\mathbf{W}(f)) = \langle \log \mathcal{P}_x(\mathbf{X}(f)|\mathbf{W}(f))\rangle_i = \log\det(\mathbf{W}(f)) + \langle \log \mathcal{P}_s\left(\mathbf{W}(f)\,\mathbf{X}(f)\right)\rangle_i, \tag{7}$$

where $\langle\cdot\rangle_i$ denotes expectation computed as the sample average over all voxels i. We perform maximization by complex gradient ascent on the likelihood-surface. The (T,T')-element $\delta w_{TT'}(f)$ of the gradient matrix $\nabla\mathbf{W}(f)$ is defined as

$$\delta w'_{TT'}(f) = \left(\frac{\partial}{\partial\Re w_{TT'}(f)} + \mathrm{i}\frac{\partial}{\partial\Im w_{TT'}(f)}\right) L(\mathbf{W}(f)), \tag{8}$$

where $\partial/\partial\Re w_{TT'}(f)$ and $\partial/\partial\Im w_{TT'}(f)$ denote differentiation with respect to the real and imaginary parts of matrix element $w_{TT'}(f)$, respectively. Using natural gradient optimization [18], this results in

$$\tilde{\nabla}\mathbf{W}(f) = \nabla\mathbf{W}(f)\,\mathbf{W}(f)^H\,\mathbf{W}(f) = \left(\mathbf{I} - \mathbf{V}(f)\,\mathbf{U}(f)^H\right)\mathbf{W}(f), \tag{9}$$

where $\mathbf{V}(f)$ is a non-linear function of the source estimates $\mathbf{U}(f)$:

$$v_{Ti}(f) = \mathrm{sign}(u_{Ti}(f))\,g(|u_{Ti}(f)|), \tag{10}$$

$$\mathrm{sign}(z) = \begin{cases} 0 & \text{if } z = 0, \\ z/|z| & \text{if } z \neq 0. \end{cases} \tag{11}$$

$\mathbf{I}$ denotes the identity matrix and the function $g(\cdot) : \mathbb{R} \to \mathbb{R}$ is a real-valued non-linearity, chosen as $g(x) = \tanh(x)$.

3 Results

The experimental data were from a 250 s experimental session consisting of ten epochs with stimulus onset asynchrony (SOA) of 25 s. An 8-Hz flickering checkerboard stimulus was presented to one subject for 3.0 s at the beginning of each epoch. The subject was requested to fixate a red cross in the center of the visual field between stimulations. 500 time-points of data were recorded at a sampling rate of 2 Hz (TR=0.5) with resolution $64 \times 64 \times 5$ voxels, field-of-view 250×250 mm^2, slice thickness 7 mm, 5 slices. fMR images were recorded with a 3 tesla Medspec 30/100 scanner (Bruker Medizintechnik GmbH, Ettlingen, Germany) at the Integrated Brain Research Unit (IBRU) of Taipei Veterans General Hospital, Taipei, Taiwan. A structural T1-weighted image with a resolution of 256×256 voxels was recorded with the same slice positions as the functional images.

In a preprocessing step, the recorded images were subjected to slice timing adjustment, which compensated for the recording time difference between individual slices. Off-brain and low-intensity voxels were identified and removed by thresholding intensities of the structural image, reducing the number of voxels in the functional images by about 86% (from 20480 to 2863). For more experiment details refer to [19]. The data of this experiment and the preprocessing routines are freely available as part of the FMRLAB toolbox for ICA analysis of fMRI data [20].

Spectral decomposition was performed using the windowed discrete Fourier transformation (1) with a Hanning window of length 40 samples, a window shift of 1 sample, and frequency-bands $0.05, 0.10, \ldots, 1.00$ Hz. This resulted in data split into 20 bands, each with 461 time-points and 2863 voxels.

Spatial complex ICA decomposition was performed within each frequency-band. In a preprocessing step, input dimensionality in each band was reduced from 461 to 50 by retaining only the subspace spanned by the (complex) eigenvectors corresponding to the 50 largest eigenvalues of the data matrix $\mathbf{X}(f)$. Complex ICA decomposed this subspace into 50 complex independent components per band.

Motivated by previous results of real-valued infomax ICA on the same data [19], we were interested in components with a region of activity (ROA) near primary visual cortex V1. One such component was found in several low-frequency spectral bands, with a time-course of activation that reflected the SOA of the visual stimulus.

Spatial and temporal activation patterns associated with visual stimulation are displayed in figures 3–10 for frequency bands 0.05 Hz, 0.10 Hz and 0.15 Hz. Being derived by complex ICA, both spatial and temporal bases are complex-valued. The spatial patterns are displayed with separate magnitude and phase plots. For the temporal activation patterns, magnitude is the most informative part and displayed here.

As can be seen from the spatial pattern magnitude plots (figures 3, 4, 6, 8), all components include activation of the primary visual area, most obvious in slices 3 and 4 of each component. This is best seen in Fig. 3, where the functional image of component IC2 in the 0.10-Hz frequency band (cf. Fig. 6) has been interpolated to higher resolution and superimposed on the structural image. The ROAs in all three frequency bands coincide remarkably well, even though complex ICA was run independently in each frequency band. Phase in the visual areas (figures 4, 7, 8) exhibits smooth changes ("gradients"), investigated in more detail below. It should be noted that smoothness

of the phase- and magnitude-variation across space is not "built-in" to the complex ICA algorithm, which rather allows arbitrary variations of phase and magnitude across neighboring voxels.

Magnitude of the complex-valued activation time-course reflects the sequence of visual stimulation in intervals of 25 s. The temporal stimulation pattern is best captured by the component in the 0.10-Hz band (Fig. 10, center), which has component number 2, i.e., it is the second-largest component in this spectral band in terms of the signal variance it explains. This component remarkably well captures exclusively the pattern of visual stimulation. The components in the 0.05-Hz and 0.15-Hz frequency bands (component numbers 16 and 9, respectivley) reflect the stimulation sequence with a lower degree of reliability, possibly a result of the smaller strength in terms of variance accounted for (Fig. 10, left and right).

Because of its ROA near V1, its strength and its reliable time-locking of component activity to stimulus presentation, we chose component number 2 (IC2) in the 0.10-Hz band for more detailed examination. Figures 3 and 6 display the magnitude of the complex spatial component map of IC2 in the ROA of the five recording slices. The ROA was determined from *z*-scores of the component map by transforming each component map to zero mean and unit variance, and setting a heuristic threshold of 1.5. The extent of IC2 from the centrally located main blood vessels to primary visual cortex is clearly visible, in particular in slices 3 and 4. The complex component's phase in the ROA is displayed in Fig. 7. Slices 3 and 4 display a phase shift from the upper left border of the component ROA image towards the lower right border. The phase shift indicates a time lag in the activation of the component voxels when transformed back into the time-domain which will be further investigated below. Fig. 10 shows magnitude of the component's time-course of activation. Component magnitude clearly reflects the pattern of visual stimulation with an SOA of 25 s, with peaks in amplitude that follow stimulation with a time lag of about 9 s, and a high dynamic range between component activity and inactivity.

Complex voxel activity induced by the component may be obtained by backprojecting the complex time-course to the complex spatial map, i.e., by forming the product $\mathbf{a}_{T'}(f)\,\mathbf{s}_{T'}(f)$, where T' denotes component number, $\mathbf{a}_{T'}(f)$ the corresponding column of the mixing matrix $\mathbf{A}(f)$, and $\mathbf{s}_{T'}(f)$ the corresponding row of the source matrix $\mathbf{S}(f)$. Transforming the complex frequency-domain voxel activity to the real time-domain reduces—in the case of a window-shift of one sample and a single frequency-band—to taking the real-part. We performed these steps to analyze time-domain voxel activity induced by the component near the largest component magnitude peak between 179.5 s and 187.0 s of the experiment. Fig. 11 displays the activity within a patch of 24 voxels located in recording slice 4, marked by a blue square in Fig. 7. Following stimulus presentation at 175.0 s, activity in the patch started to increase with a time lag of about 4.5 s, first in the voxels most centrally located in the brain (top row of voxels in each plot of Fig. 11), and propagating within about 1 s to the posterior voxels of to primary visual cortex (bottom row in each plot of Fig. 11). Analogously, voxel activity decreased first in the top row of voxels before decreasing in the bottom rows.

To investigate whether similar time lag effects can be found *without* ICA processing, we also computed the 0.10-Hz band activity of the recorded data at the 24 voxels that

have been investigated in Fig. 11, using the same spectral decomposition that has been used for the complex ICA decomposition. Activity accounted for by recorded data and by IC2 was separately averaged within each voxel row, starting with row 1 for the most centrally located voxels, and up to row 6 for the voxels in the posterior position. The resulting averages are plotted in Fig. 12 for recorded data and for component induced activity. Since the signals are band-limited, we obtain oscillatory activity with positive and negative swings. The analysis of relative time lags and amplitudes near the peak of component magnitude (at 184.5 s) is not influenced by this fact. In the component induced activity, the more centrally located voxels are activated between 0.5 s and 1.0 s prior to the posterior voxels. The time lag increases monotonously with more posterior voxel position. This gradient of posterior voxels being activated later than the central voxels is also reflected in the activity of the recorded voxels signals. However, the voxels in row 3 form an exception since their extremal activation occurs even after the posterior voxels are activated. The analysis of activation amplitudes in Fig. 12 gives similar results: The component induced amplitude increases monotonously towards more posterior voxel position. Overall, this tendency is also found in the recorded signals, but some exceptions occur, e.g., amplitude in row 2 is smaller than in row 1.

To compare the complex ICA results with those obtained by standard ICA, real-valued infomax ICA as implemented in the FMRLAB toolbox [19] was applied to the same data in the time-domain. Among the resulting independent components, we found one (and only one) component whose ROA (Fig. 13) highly matches the ROA of the complex ICA components accounting for visual area activity, as presented in Figures 3 to 9. The same vision-related physiological process is modeled by the different algorithms, albeit the spatio-temporal dynamics necessarily is neglected in the model obtained with standard ICA. This example indicates that complex convolutive ICA is not only a generalization of standard ICA in terms of the underlying mathematics. It may also be regarded as a generalization in terms of results obtained from real-world data where complex ICA identifies similar underlying processes and models them at greater detail.

A component obtained by complex ICA pertaining a non-vision related process is displayed in Fig. 14. The component ROA in the 0.05-Hz band clearly reflects activity related to cerebrospinal fluid (CSF) in ventricular areas. Hence, complex ICA successfully isolates flow artifacts from CSF activity into a separate component. Similar components are often observed in standard ICA decompositions of fMRI data and are also present in the decomposition of this dataset with real-valued ICA (data not shown here), reinforcing the view that complex ICA finds components generated by the same physiological processes that are extracted by real-valued ICA analysis. Any residual overlap of the previously discussed vision-related components with ventral areas is attributed to a partial volume effect of the brain voxels surrounding ventral areas and to the spatial resolution of the fMR image acquisition.

4 Discussion and conclusion

We analyzed fMRI signals using a convolutive ICA approach which enabled us to model patterns of spatio-temporal dynamics. Parameters for this model were efficiently esti-

mated in the frequency-domain where the convolution factorizes into a product. Our method consists of three processing stages: 1) Computing time-frequency representations of the recorded signals, using short-term Fourier transformation. 2) Separation of the measured signals into independent components using spatial complex infomax ICA in each frequency-band. 3) Computing the corresponding dynamic voxel activation pattern induced by each independent component in the time-domain.

From data of a visual stimulation fMRI experiment we obtained complex components in the 0.05-Hz, 0.10-Hz and 0.15-Hz bands with component map ROAs extending across primary visual cortex and its blood supply vessels. The spatial extent of the components was remarkably similar across frequencies, showing that these components captured a single physiological source's properties in different spectral bands.

In-depth analysis focused on the component obtained in the 0.10-Hz band. By reconstructing the spatio-temporal activation pattern accounted for by this component, we identified a time lag of about 1 s between activation of central and posterior voxels. A related time lag, but distributed less regularly, could be observed in the 0.1-Hz frequency-band of the measured signals. The amplitude of component-induced voxels activations increased in the posterior direction. Also this trend could be seen in the recorded signals, but it was less systematic than for the ICA processed signals.

Both observations are compatible with the physiology underlying generation of the fMRI signal. The posterior voxels in the component ROA are the ones closest to the posterior drainage vein. The convergence of over-supplied oxygenated blood towards the drainage vein may therefore result in the large amplitudes for these voxels. The temporal delay between activation of central and posterior voxels is consistent with the propagation of over-supplied oxygenated blood from the centrally located arteries to the posterior drainage vein. Similar temporal delays have been observed from optical recordings of intrinsic signals, related to blood oxygenation, in monkey visual cortex [21].

These results may indicate that frequency-domain complex infomax ICA can capture patterns of spatio-temporal dynamics in the data. It is reassuring that similar dynamics could also be observed in the recorded (mixed) signals, making the possibility of the complex ICA results being mere processing artifacts implausible. On the other hand, the spatio-temporal dynamics emerged with a higher degree of regularity and physiological plausibility from the complex ICA results than from the measured data. Separation of the stimulus evoked activity from interfering, ongoing brain activity by the complex ICA method appears as the natural explanation for this observation.

Here, we have focused on the analysis of individual frequency-bands. Combining the extracted information across several frequency-bands in which components have been found near V1 should allow us to reconstruct the full time-domain spatio-temporal dynamics associated with visual stimulation.

In conjunction with previous results reported on modeling the spatio-temporal dynamics in EEG signals with complex ICA [3], the results presented here are a further indication that convolutive models may be useful for analyzing a wide range of data.

Acknowledgements

We acknowledge support by the German Research Council DFG (J. A.), and by the Swartz Foundation.

References

1. Martin J. McKeown, Scott Makeig, Greg G. Brown, Tzyy-Ping Jung, Sandra S. Kindermann, Anthony J. Bell, and Terrence J. Sejnowski. Analysis of fMRI data by blind separation into independent spatial components. *Human Brain Mapping*, 6:160–188, 1998.
2. M. J. McKeown, T.-P. Jung, S. Makeig, G. Brown, S. S. Kindermann, T. W. Lee, and T. J. Sejnowski. Spatially independent activity patterns in functional MRI data during the Stroop color-naming task. *Proc. Natl. Acad. Sci. U. S. A.*, 95:803–810, 1998.
3. J. Anemüller, T. J. Sejnowski, and S. Makeig. Complex independent component analysis of frequency-domain electroencephalographic data. *Neural Networks*, 16:1311–1323, 2003.
4. Lucas Parra and Clay Spence. Convolutive blind separation of non-stationary sources. *IEEE Transactions on Speech and Audio Processing*, 8:320–327, 2000.
5. J. Anemüller. *Across-Frequency Processing in Convolutive Blind Source Separation*. PhD thesis, Dept. of Physics, University of Oldenburg, Oldenburg, Germany, 2001.
6. H. Buchner, R. Aichner, and W. Kellermann. A generalization of blind source separation algorithms for convolutive mixtures based on second-order statistics. *IEEE transactions on speech and audio processing*, 13:120–134, 2005.
7. J. V. Stone, J. Porrill, N. R. Porter, and I. W. Wilkinson. Spatiotemporal independent component analysis of event-related fMRI data using skewed probability density functions. *NeuroImage*, 15:407–421, 2002.
8. J. Anemüller and B. Kollmeier. Adaptive separation of acoustic sources for anechoic conditions: A constrained frequency domain approach. *Speech Communication*, 39(1-2):79–95, Jan 2003.
9. A. J. Bell and T. J. Sejnowski. An information maximization approach to blind separation and blind deconvolution. *Neural Computation*, 7:1129–1159, 1995.
10. Jörn Anemüller and Tino Gramß. On-line blind separation of moving sound sources. In J. F. Cardoso, Ch. Jutten, and Ph. Loubaton, editors, *Proceedings of the first international workshop on independent component analysis and blind signal separation*, pages 331–334, Aussois, France, 1999.
11. Jean-François Cardoso and Beate Hvam Laheld. Equivariant adaptive source separation. *IEEE Transactions on Signal Processing*, 44:3017–3030, 1996.
12. H. Sawada, R. Mukai, S. Araki, and S. Makino. A polar-coordinate based activation function for frequency domain blind source separation. In T.-W. Lee, T.-P. Jung, S. Makeig, and T. J. Sejnowski, editors, *Proceedings of the 3rd international conference on independent component analysis and blind signal separation*, pages 663–668, 2001.
13. H. Sawada, R. Mukai, S. Araki, and S. Makino. Polar coordinate based nonlinear function for frequency-domain blind source separation. *IEICE Transactions*, E86-A:590–596, 2003.
14. J.-F. Cardoso and A. Souloumiac. Blind beamforming for non Gaussian signals. *IEE Proceedings F*, 140:362–370, 1993.
15. E. Bingham and A. Hyvärinen. A fast fixed-point algorithm for independent component analysis of complex valued signals. *International Journal of Neural Systems*, 10:1–8, 2000.
16. V. D. Calhound, T. Adali, G. D. Pearlson, P. C. van Zijl, and J. J. Pekar. Independent component analysis of fMRI data in the complex domain. *Magnetic Resonance in Medicine*, 48:180–192, 2002.

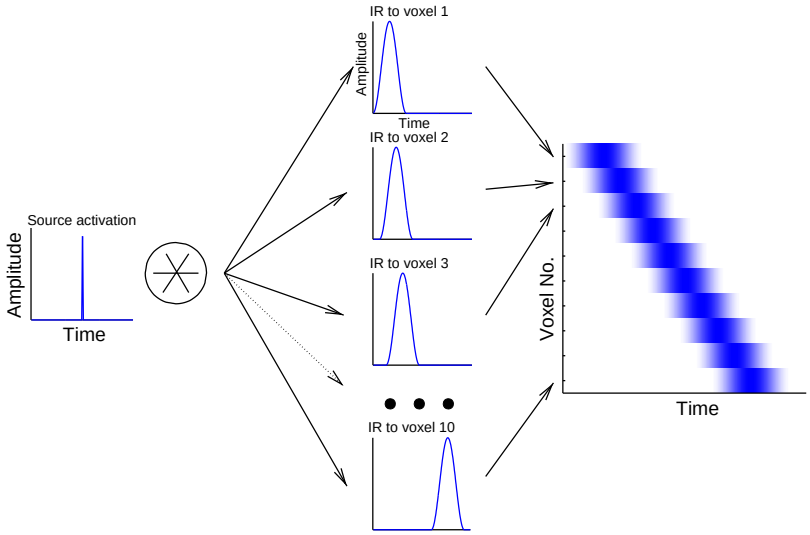

Fig. 1. Spatio-temporal dynamics generated by a toy-example convolution model. An idealized, delta-shaped source activation (left) is convolved with several impulse responses ("IR", center) which project the source activation to different fMRI voxels arranged on a line (right). Different time-lags and the temporal "smearing" introduced by the impulse responses result in the measurement of a spatio-temporal pattern at the voxels which is spatially extended and moves across the voxel array. By varying the impulse responses used, more complex spatio-temporal patterns may easily be generated.

17. S. Fiori. Non-linear complex-valued extensions of hebbian learning: an essay. *Neural Computation*, 17:779–838, 2005.
18. S. Amari, A. Cichocki, and H. H. Yang. A new learning algorithm for blind signal separation. In D. Touretzky, M. Mozer, and M. Hasselmo, editors, *Advances in Neural Information Processing Systems 8*, pages 757–763, Cambridge, MA, 1996. MIT Press.
19. Jeng-Ren Duann, Tzyy-Ping Jung, Wen-Jui Kuo, Tzu-Chen Yeh, Scott Makeig, Jen-Chuen Hsieh, and Terrence J. Sejnowski. Single-trial variability in event-related BOLD signals. *NeuroImage*, 15:823–835, 2002.
20. J.-R. Duann, T.-P. Jung, and S. Makeig. FMRLAB: Matlab software for independent component analysis of fMRI data. World Wide Web publication, 2003. http://sccn.ucsd.edu/fmrlab.
21. R. M. Siegel, J. R. Duann, T. P. Jung, and T. J. Sejnowski. Independent component analysis of intrinsic optical signals for gain fields in inferior parietal cortex of behaving monkey. In *Society for Neuroscience Abstracts 28*, 2002.

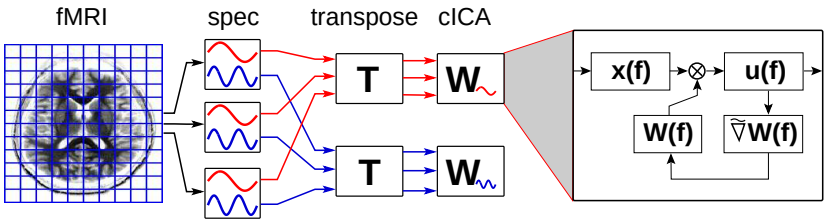

Fig. 2. Schematic representation of the processing steps of the complex frequency-domain ICA algorithm. Voxel time-courses are recorded with an fMRI scanner ("fMRI"). The corresponding time-frequency representation is computed for each voxel using a (temporal) short-term Fourier tranformations ("spec"). In order to apply the complex ICA a spatial (as opposed to temporal) decomposition mode, the data is rearranged ("transpose") so that number of short-term temporal windows determines input dimenationality and number of voxels determines samples. Complex ICA is performed within each spectral band ("cICA"). The iteration steps of the complex ICA algorithm are depicted on the right.

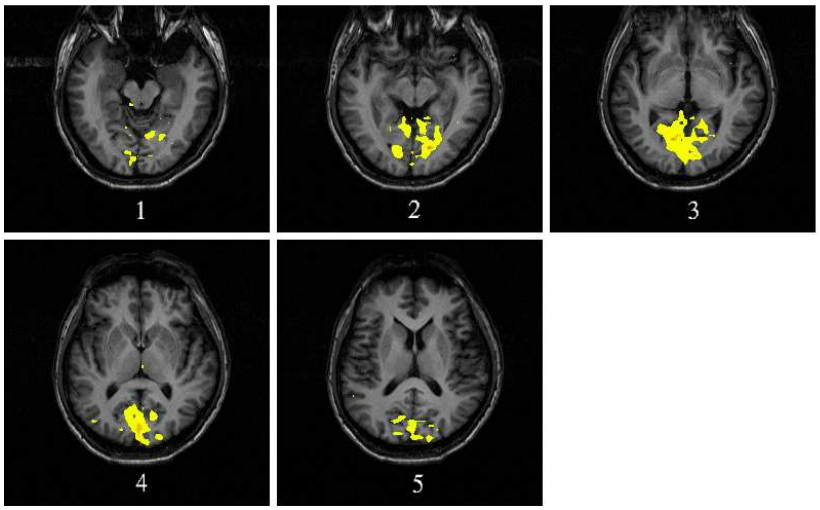

Fig. 3. Magnitude map of the component region of activity (ROA) for complex component IC2 obtained by complex ICA in the 0.1-Hz frequency-band. The ROA extends over visual area V1 and blood supply vessels. Colors indicate component magnitude in the ROA. The structural image of the recorded areas is plotted in darker gray tones. The component ROA is interpolated to the higher resolution of the structural scan for better visualization. (Note: The electronic version of this document contains color figures for better visualization and can be obtained from the first author.)

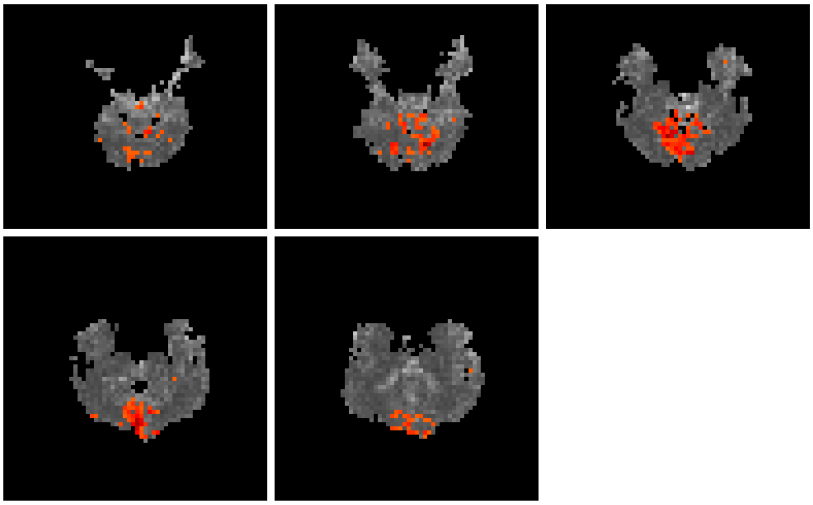

Fig. 4. Magnitude map of the component ROA for complex component IC16 in the 0.05-Hz band. Colors indicate component magnitude in region of activity. Note that in contrast to Fig. 3 the information is displayed at the lower spatial resolution of the functional recordings.

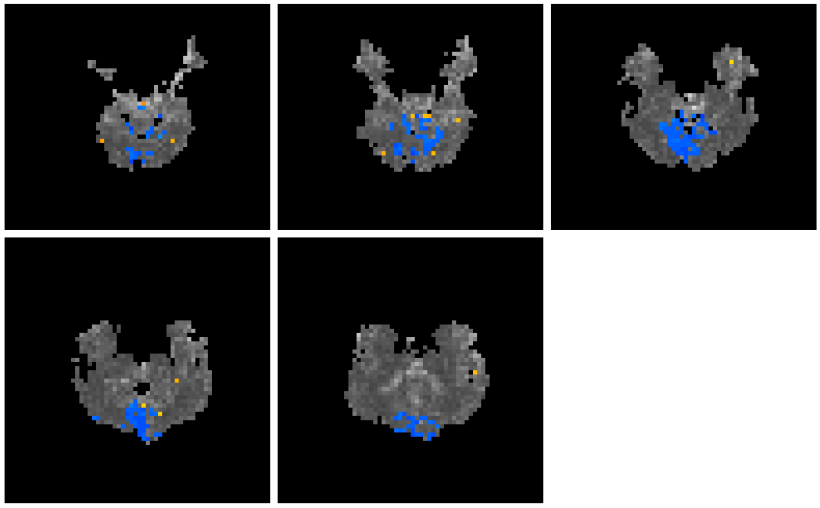

Fig. 5. Phase map of the component ROA for complex component IC16 in the 0.05-Hz band, corresponding to the magnitude map displayed in Fig. 4. Colors indicate component phase in region of activity.

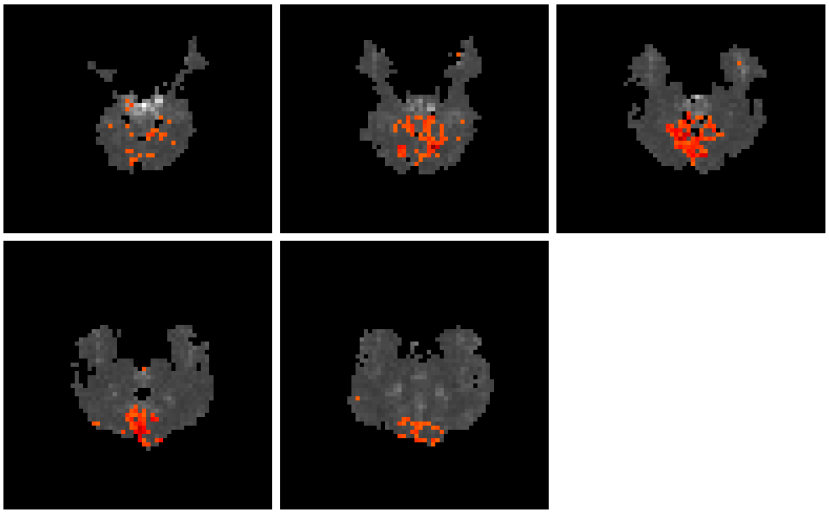

Fig. 6. Magnitude map of the component ROA for complex component IC2 in the 0.10-Hz frequency-band. Colors indicate component magnitude in the ROA. The plot contains the same information as displayed in Fig. 3, but shown at the lower resolution of the functional scans and with a different colormap.

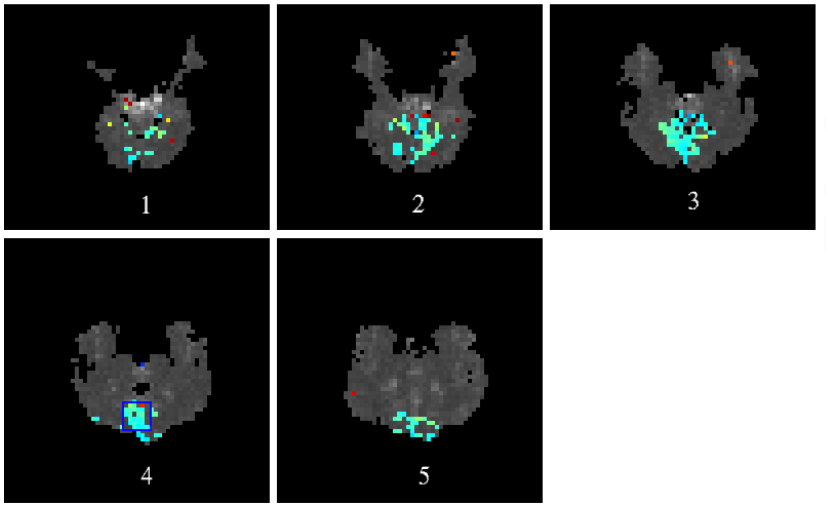

Fig. 7. Phase map of the component ROA for complex component IC2 in the 0.10-Hz band, corresponding to the magnitude map displayed in Fig. 6. Colors indicate component phase in the ROA. The voxels marked by a blue square in slice 4 are investigated further in Fig. 11.

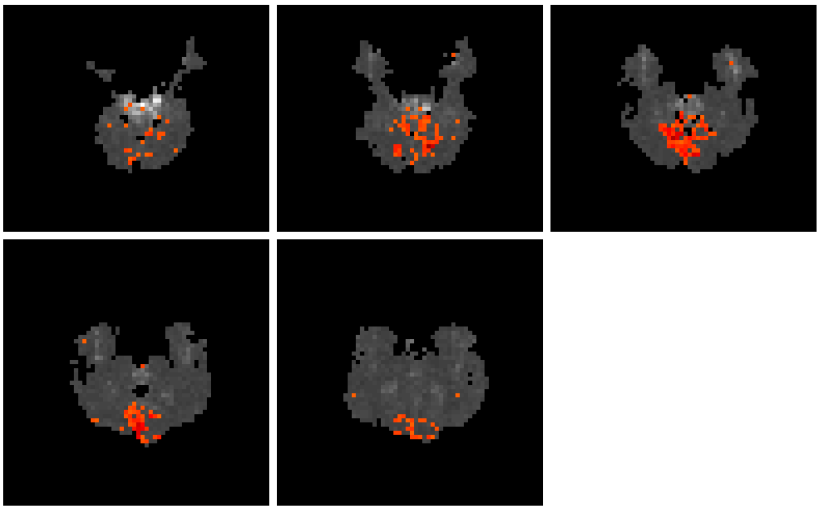

Fig. 8. Magnitude map of the component ROA for complex component IC9 in the 0.15-Hz frequency-band. Colors indicate component magnitude in the ROA.

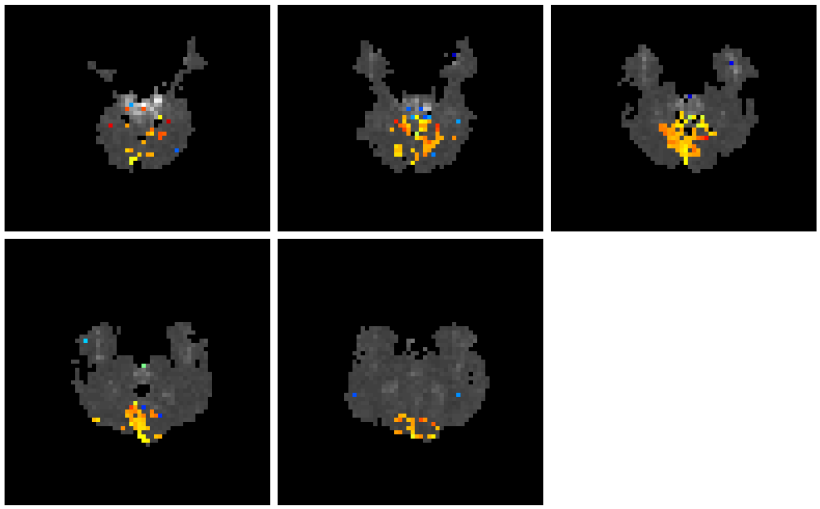

Fig. 9. Phase map of the component ROA for complex component IC9 in the 0.15-Hz band, corresponding to the magnitude map displayed in Fig. 8. Colors indicate component phase in the ROA.

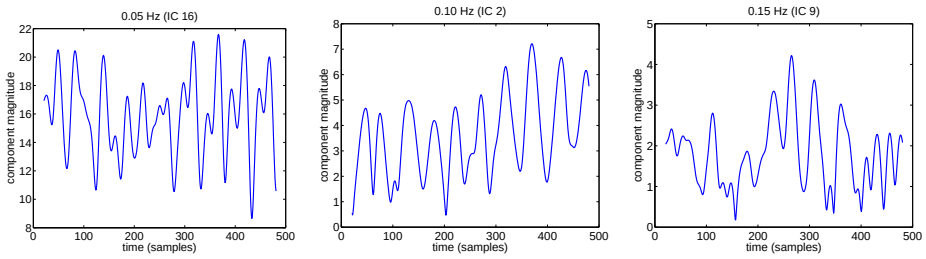

Fig. 10. Time-course of component magnitude of complex component IC16 in the 0.05-Hz frequency-band (left), component IC2 at 0.10 Hz (center) and component IC9 at 0.15 Hz (right). Note the time-locking of amplitude and phase to stimulus presentation in 25 seconds intervals, in particular in component IC2 at 0.10 Hz. The first and last 10 seconds of the experiment are not shown because computation of the spectral components was stopped when the analysis window (length 20 s) reached the edges of the recording. The time-interval from 179.5 s to 187.0 s around the largest component magnitude peak of IC2 (center) is investigated further in figure 11.

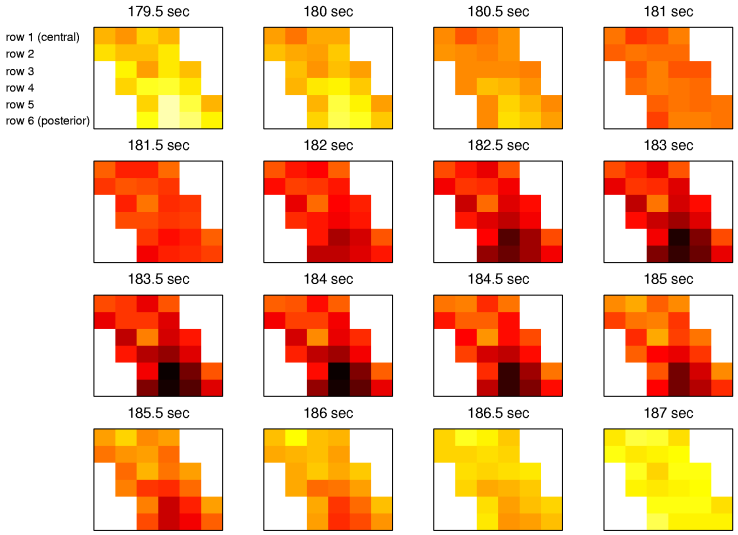

Fig. 11. Backprojected component activity from complex component IC2. Complex component time-course was backprojected to corresponding activity at the voxels and transformed to the time-domain. Shown is the activity of 24 voxels in visual area V1, the position of which is marked by a blue box in slice 4 of Fig. 7. The flickering-checkerboard stimulus was presented for 3.0 s at experiment time 175.0 s (not shown). Activation started to increase with a time lag of about 4.5 s, with first increase occuring at the centrally-located voxels (top rows), and propagated to the posterior voxels (bottom rows) within approximately 1 s. This is compatible with over-supplied oxygenated blood propagating in the posterior direction and being washed out through the drainage vein from area V1.

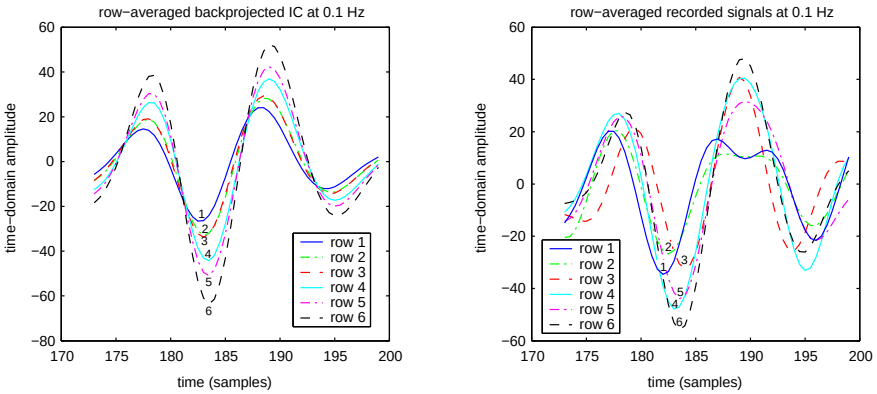

Fig. 12. Left: Average time-courses near largest component power peak (at 184.5 s) for each row of 0.1-Hz band time-domain backprojected component activations displayed in Fig. 11. Row 1 corresponds to the most centrally located voxels, row 6 to the posterior ones. Right: Corresponding average time-courses computed from the recorded activations in the 0.1-Hz band of the same voxels. For the average IC activation (left), the voxel-rows are activated in the order $1-(2,3)-(4,5,6)$ with row 6 being activated with a time lag of about 1 second with respect to row 1. This lag is compatible with blood supply propagating across the patch in the posterior direction. In the average recorded activations (right), the voxel-rows are activated in the order $1-2-4-(5,6)-3$. With the exception of row 3, this also indicates a posterior direction of propagation. The most posterior voxel-row of backprojected component IC2 shows strongest activation which is plausible since it is closest to the drainage vein. The same tendency is found in the recorded signals, but ordering of amplitude of voxel-rows is not as monotonous as for IC2. Backprojected IC activations may represent a cleaner picture of the stimulus related process with respect to phase- and amplitude-gradient, because activity of other ongoing brain processes is canceled out.

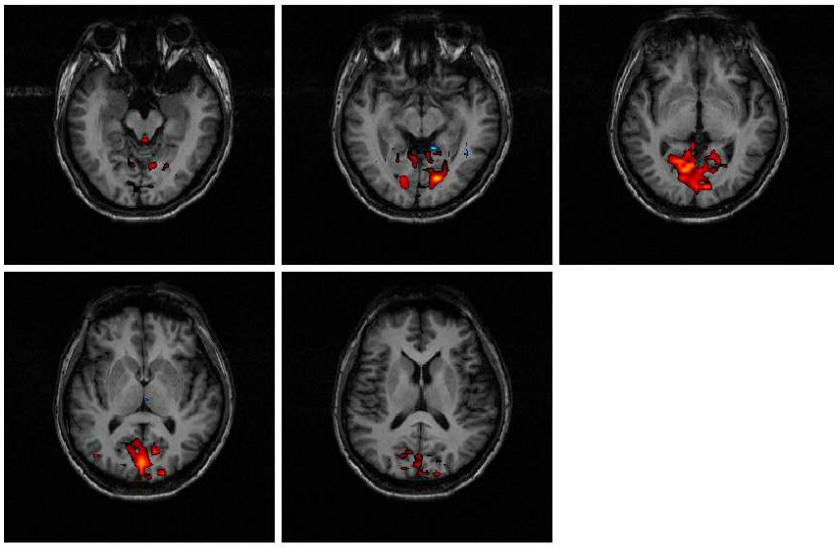

Fig. 13. Comparison with results from standard ICA. ROA of component IC8 obtained with real-valued infomax ICA, superimposed on the structural image and ROA interpolated to the higher resolution of the structural scan. Similar to the components from complex ICA, this component extends over visual area V1 and blood supply vessels. The large overlap between the real-valued component and the complex-valued components shown in Figs. 3 to 9 shows that they model the same physiological (visual) process, although the real-valued component cannot take into account the spatio-temporal dynamics reflected in the complex ICs.

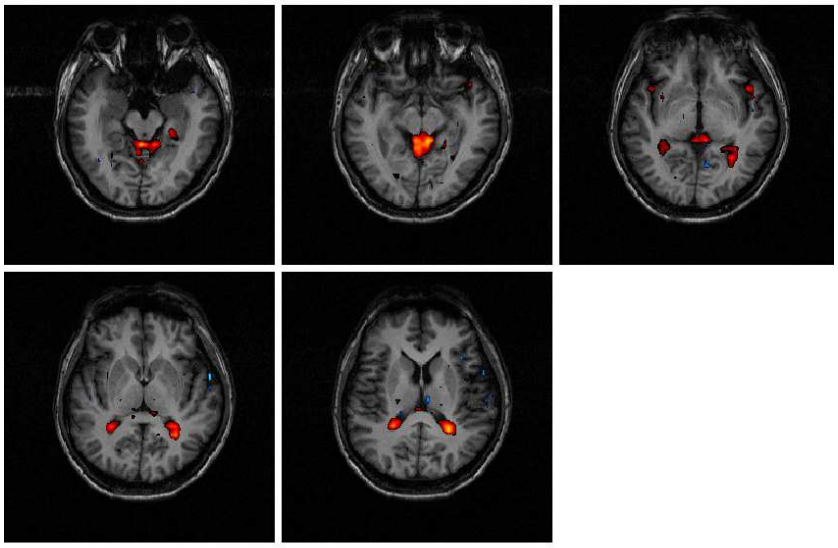

Fig. 14. Complex ICA component reflecting cerebro-spinal-fluid (CSF) activity in ventral areas. Magnitude map of the component ROA for complex component IC1 in the 0.05-Hz band, superimposed on structural image and interpolated to its higher resolution.